Fast Ionic Conductivity in the Most Lithium-Rich Phosphidosilicate $Li_{14}SiP_6$

Stefan Strangmüller,[a, ‡] Henrik Eickhoff,[a, ‡] David Müller,[a] Wilhelm Klein,[a] Gabriele Raudaschl-Sieber,[a] Holger Kirchhain,[b] Christian Sedlmeier,[c] Volodymyr Baran,[d] Anatoliy Senyshyn,[d] Volker L. Deringer,[e] Leo van Wüllen,[b] Hubert A. Gasteiger,[c] and Thomas F. Fässler*,[a]

[a]Department of Chemistry, Technische Universität München, Lichtenbergstrasse 4, D-85747 Garching, Germany

[b]Department of Physics, University of Augsburg, Universitätsstrasse 1, D-86159 Augsburg, Germany

[c]Department of Chemistry, Technische Universität München, Lichtenbergstrasse 4, D-85747 Garching, Germany

[d]Heinz Maier-Leibnitz Zentrum, Technische Universität München, Lichtenbergstrasse 1, D-85748 Garching; Germany

[e]Department of Engineering, University of Cambridge, Cambridge CB2 1PZ, United Kingdom

KEYWORDS: Lithium ion conductor, Crystal structure, Phosphidosilicate, Ball mill, 3D Diffusion pathways, Neutron Diffraction.

ABSTRACT: Solid electrolytes with superionic conductivity are required as a main component for all-solid-state batteries. Here we present a novel solid electrolyte with three-dimensional conducting pathways based on "lithium-rich" phosphidosilicates with ionic conductivity of $\sigma > 10^{-3}$ S cm^{-1} at room temperature and activation energy of 30-32 kJ mol^{-1} expanding the recently introduced family of lithium phosphidotetrelates. Aiming towards higher lithium ion conductivities systematic investigations of lithium phosphidosilicates gave access to the so far lithium-richest compound within this class of materials. The crystalline material (space group $Fm\bar{3}m$), which shows reversible thermal phase transitions, can be readily obtained by ball mill synthesis from the elements followed by moderate thermal treatment of the mixture. Lithium diffusion pathways via both, tetrahedral and octahedral voids, are analyzed by temperature-dependent powder neutron diffraction measurements in combination with maximum entropy method (MEM) and DFT calculations. Moreover, the lithium ion mobility structurally indicated by a disordered Li/Si occupancy in the tetrahedral voids plus partially filled octahedral voids, is studied by temperature-dependent impedance and ^{7}Li NMR spectroscopy.

1. Introduction

All-solid-state battery technology is currently attracting considerable interest, as such batteries possess a number of potential advantages over liquid electrolyte systems, including energy density gains and improved safety. As a consequence, a large number of inorganic materials with both crystalline and amorphous structures as well as their composite structures have been investigated experimentally and theoretically as potential solid electrolyte candidates.[1-2] In particular the investigation of lithium ion solid electrolytes in lithium ion batteries (LIBs) has increased rapidly in order to improve the performance of electrochemical energy storage systems.[3]

In order to achieve a significant ionic conductivity in a crystalline solid, at first a high charge carrier density should coincide with a large number of available lattice sites. Secondly, solid electrolytes require a low activation energy for lithium mobility as it is found in materials in which cation sites are arranged in face-sharing polyhedra that are formed by anions.[4] For example, for garnet-type solid electrolytes the effect of polyhedral connectivity on the ionic conductivity has been shown recently.[5] A large polarizability of the anions has been suggested as another factor for lowering the activation barrier for Li^+ mobility,[6] and accordingly sulfides, thiophosphates and materials containing iodine such as Li-argyrodites are investigated as superionic conductors.[7-14] E.g. Li_3PS_4 shows an ionic conductivity which is several orders of magnitudes higher than that of Li_3PO_4, and the same applies for Li_6PS_5Cl versus Li_6PO_5Cl.[15-16] The best superionic conductors are found if a combination of several of these aspects appear as observed e.g. in $Li_{10}GeP_2S_{12}$ (LGPS), which can formally be regarded as variation of pristine Li_3PS_4, combined with the Li-richer Li_4GeS_4 [$Li_{10}(GeS_4)(PS_4)_2$ = 2 Li_3PS_4 + Li_4GeS_4], or in the argyrodites Li_6PS_5X, which formally represent a combination of Li_3PS_4, Li_2S and LiX [$Li_6(PS_4)(S)X$ = Li_3PS_4 + Li_2S + LiX].[6,10]

Following these concepts we recently started to reinvestigate the ternary phase systems Li-Si-P and Li-Ge-P[17] and found ionic conductivities up to 10^{-4} S cm^{-1} at room temperature for pure Li_8SiP_4 and Li_8GeP_4.[18-19] Li_8SiP_4, comprising discrete $[SiP_4]^{8-}$ tetrahedra, fulfills most of the criteria mentioned above: a) It has more than twice the Li^+ concentration of Li_3PS_4; b) the higher formal charge of minus two at the P atoms in the $[SiP_4]^{8-}$ units hints for a higher polarizability than the formally one-fold negatively charged sulfur atoms in PS_4^{3-} and c) most intriguingly, the crystal structure of Li_8SiP_4 is closely related to the anti-structure type of CaF_2. The atom packing of Li_8SiP_4 derives from cubic close packing (*ccp*) of the P atoms which in consequence creates eight tetrahedral and four octahedral voids per formula unit. Out of these twelve voids only one tetrahedral site is filled by a Si atom which can be considered as covalently

bound to the four P atoms. In addition eight Li atoms per formula unit can be distributed within the remaining 11 voids and, thus, numerous empty vacancies for a possible Li^+ hopping are present. As an additional advantage in the *ccp*, tetrahedral and octahedral voids share common faces, a fact that enlarges the window for diffusion pathways, compared to edge-sharing polyhedra.[20-21] This concept of cation disorder in lithium phosphidotetrelates should create a promising opportunity to get access to high-performance lithium ion conductors, which has already been successfully applied to the Li-Ge-P system, as indicated by the close structural relationship between Li_8SiP_4 and α- and β-Li_8GeP_4.[19]

However, the Li^+ conductivity can even be further increased by using different or disordered anions. The presence of differently charged anions may allow for a fine-tuning of the Li^+ concentration within the compound, and a disorder may reduce the activation barrier.[22-23] A well-established example for lithium ion conductors in which all these concepts are realized is the recently discovered class of Li-argyrodites Li_6PS_5X (X = Cl, Br, I). Their cubic crystal structure ($F\bar{4}3m$) consists of two different types of anionic building blocks, tetrahedral $[PS_4]^{3-}$ units and isolated S^{2-} or X^- ions in the ratio 1:2, separated by lithium ions.

We now apply the concept of increased disorder over a larger number of polyhedral voids on one hand, and of an increased overall Li^+ mobility on the other, to lithium phosphidosilicates (LSiP). The formal addition of more Li-rich Li_3P to one equivalent of Li_8SiP_4 corresponds to a line through Li_3P and Li_8SiP_4[18] in the ternary composition diagram Li-Si-P (Figure 1). Interestingly, at the Li-poor side along this line several compounds such as $Li_{10}Si_2P_6$,[24] Li_2SiP_2,[18, 25] and $LiSi_2P_3$[25] are already known. The line hits the binary border at a nominal stoichiometry of "Si_3P_4".

Here we report on a new compound with a higher Li content than Li_8SiP_4 obtained by a formal addition of Li_3P. Based on the crystal structures of Li_8SiP_4 and Li_3P, one might expect the presence of $[SiP_4]^{8-}$ and P^{3-} as anionic building units similar to the simultaneous appearance of $[PS_4]^{3-}$ and S^{2-} in Li-argyrodites. We found a straightforward and simple synthesis route for the new phosphidosilicate $Li_{14}SiP_6$, which shows the highest Li^+ density among the more complex lithium ion conductors. This route leads to a crystalline material and comprises mechanochemical ball milling of the elements with subsequent annealing of the mixture. The crystal structure was determined by single crystal and by powder X-ray, as well as by powder neutron diffraction methods. The purity of the samples was confirmed by elemental analyses as well as by solid state ^{6}Li, ^{29}Si and ^{31}P MAS NMR spectroscopy. The thermal properties of the material were studied by differential scanning calorimetry and temperature-dependent powder neutron diffraction experiments. Finally, the Li^+ migration has been investigated by electrochemical impedance spectroscopy, temperature-dependent ^{7}Li NMR spectroscopy, high-temperature neutron diffraction measurements (maximum entropy method), and density functional theory calculations.

2. Experimental Methods

Synthesis. All syntheses were carried out under Ar atmosphere in glove boxes (MBraun, 200B) with moisture and oxygen levels below 0.1 ppm, or in containers, which were sealed under Ar atmosphere and vacuum ($< 2 \cdot 10^{-2}$ mbar), respectively. Lithium phosphidosilicates are sensitive to oxygen and moisture; in particular, contact with water results in a vigorous reaction including the formation of flammable and toxic gases (e.g. phosphine). Therefore, disposal must be carried out in small amounts at a time and under proper ventilation.

Synthesis of polycrystalline $Li_{14}SiP_6$. The synthesis route includes two steps, using stoichiometric amounts of lithium (Rockwood Lithium, 99%), silicon (Wacker, 99.9%) and red phosphorus (Sigma Aldrich, 97%) aiming for the compositions $Li_{11}SiP_5$, $Li_{14}SiP_6$, $Li_{17}SiP_7$ and $Li_{20}SiP_8$. In the first step a reactive mixture (m = 1.5-5.0 g) is prepared by mechanochemical milling using a Retsch PM100 Planetary Ball Mill (350 rpm, 36 h, 10 min interval, 3 min break) with a tungsten carbide milling jar (V = 50 mL) and three balls with a diameter of 15 mm.

In the second step, the obtained reactive mixture was pressed to pellets, sealed in batches of 0.3 to 3.0 g in carbon-coated silica glass ampoules and heated in a muffle furnace (Nabertherm, L5/11/P330) to 973 K (heating rate: 4 K min^{-1}) followed by quenching of the hot ampoules in water. Annealing times between 6-18 h yielded products with high purity. The sample used for determination of the ionic conductivity was quenched after 9 h.

Powder X-ray Diffraction. Data were collected at room temperature on a STOE Stadi P diffractometer (Ge(111) monochromator, Cu $K_{\alpha1}$ radiation, λ = 1.54056 Å or Mo $K_{\alpha1}$ radiation, λ = 0.70932 Å) with a Dectris MYTHEN 1K detector in Debye-Scherrer geometry. Samples were sealed in glass capillaries (Ø 0.3 mm) for measurement. Raw data were processed with WinXPOW[26] software prior to further refinement.

Powder Neutron Diffraction. Elastic coherent neutron scattering experiments were performed on the high-resolution powder diffractometer SPODI at the research reactor FRM-II (Garching, Germany).[27] Monochromatic neutrons (λ = 1.5482 Å) were obtained at a 155° take-off angle using the (551) reflection of a vertically-focused composite Ge monochromator. The vertical position-sensitive multidetector (300 mm effective height) consisting of 80 ^{3}He tubes of 1 inch in diameter and covering an angular range of 160° 2θ was used for data collection. Measurements were performed in Debye-Scherrer geometry. The powder sample (ca. 2 cm^3 in volume) was filled into a Nb tube container (10 mm diameter, 0.5 mm wall thickness) under argon and welded using an arc-melting apparatus. The Nb container with the sample was mounted in the top-loading closed-cycle refrigerator. ^{4}He was used as a heat transmitter. The instantaneous temperature was measured using two thin film resistance cryogenic temperature sensors Cernox and controlled by a LakeShore340 temperature controller. Two dimensional diffraction data were collected at fixed temperatures in the range of 4-300 K using 20 K temperature steps upon heating and then corrected for geometrical aberrations and the curvature of the Debye-Scherrer rings.

For measurements at high temperature the Nb container with the sample was mounted in the vacuum furnace equipped with Nb heating elements. Measurements and temperature control were carried out using two Type L thermocouples and a Eurotherm 2400 controller. The data were collected in the temperature range 297-1023 K using a temperature increment of 50 K. At temperatures below 573 K, ^{4}He was used as a thermal exchange medium, whereas at higher temperatures the furnace regulation was achieved using an isolation vacuum.

Rietveld Refinement. The data analysis was performed using the full profile Rietveld method implemented in the FullProf program package.[28] For the shaping of the peak profile, the pseudo-Voigt function was chosen. The background contribu-

tion was determined using a linear interpolation between selected data points in non-overlapping regions. The scale factor, zero angular shift, profile shape parameters, resolution (Caglioti) parameters, asymmetry and lattice parameters as well as fractional coordinates of atoms and their displacement parameters were varied during the fitting.

In accordance with the composition gained from elemental analyses the stoichiometry was set to $Li_{14}SiP_6$ (Z = 0.67) or $Li_{2.33}Si_{0.17}P$ (Z = 4), respectively. Besides the Nb reflections only reflections consistent with cubic symmetry and face centering, according e.g. to the space group $Fm\bar{3}m$ (no. 225) of antifluorite, are present in the neutron diffraction patterns. The diffraction intensities of $Li_{14}SiP_6$ have been modelled with the P atoms located at the 4*a* site and a mixed Li/Si site occupation of the residual 4*b* and 8*c* sites. Constraining the overall Li and Si concentrations to the ones from elemental analyses, along with the assumptions of full 8*c* site occupation it can be concluded that the 8*c* site is fully occupied by Si and Li, and that there is no Si located on the 4*b* site.

A joint Rietveld refinement of the powder neutron diffraction data at 300 K and of the Mo powder X-ray diffraction data at the same temperature with a single structural model was carried out approving the accuracy of the two methods. All structures were visualized using VESTA.[29]

Single Crystal X-ray Structure Determination. Single crystals of $Li_{14}SiP_6$ were obtained by a high-temperature reaction of the reactive mixture in a corundum crucible, which was sealed in a steel ampoule under Ar. The pressed sample was annealed for 6 h at 1273 K (heating rate: 4 K min^{-1}), slowly cooled to 973 K (cooling rate: 0.05 K min^{-1}) and quenched after another 8 h in water.

A single crystal of $Li_{14}SiP_6$ was isolated and sealed in a glass capillary (0.1 mm). For diffraction data collection, the capillary was positioned in a 150 K cold N_2 gas stream. Data collection was performed with a STOE StadiVari (Mo $K_{\alpha1}$ radiation) diffractometer equipped with a DECTRIS PILATUS 300 K detector. The structure was solved by Direct Methods (SHELXS-2014) and refined by full-matrix least-squares calculations against F^2 (SHELXL-2014).[30]

Elemental Analyses. Elemental analyses were performed by the microanalytical laboratory at the Department of Chemistry of the Technische Universität München. The amount of lithium in the samples was analyzed via atomic absorption spectroscopy using a 280FS AA spectrometer (Agilent Technologies). The amount of phosphorous was determined by photometry applying both the vanadate method and the molybdenum blue method, leading to almost identical values. The amount of silicon was also determined photometrically via silicon molybdate. To overcome disturbances of phosphorous and lithium, blank tests have been applied to calculate occurring deviations. The corresponding photometric analyses were carried out using a Cary UV-Vis spectrometer (Agilent Technologies).

The analyses reveal the following composition: lithium 29.4%, silicon 8.23% and phosphorus 57.89% (vanadate method) or 57.68% (molybdenum blue method). The observed overall loss of about 5% maybe caused by abrasion of small amounts of WC during ball milling and impurities within the educts (e.g. purity of Li ≥ 99% or P ≥ 97%) or formation of volatile decomposition products. Conversion and scaling of the determined values result in a stoichiometry of $Li_{13.64}Si_{0.94}P_6$.

Differential Scanning Calorimetry (DSC). For the investigation of the thermal behavior of the compounds a Netzsch DSC 404 Pegasus device was used. Niobium crucibles were filled with the samples and sealed by arc-welding. Empty sealed crucibles served as a reference. Measurements were performed under an Ar flow of 75 mL min^{-1} and a heating/cooling rate of 10 K min^{-1}. Data collection and handling was carried out with the Proteus Thermal Analysis program.[31]

Solid-State NMR Spectroscopy. Magic angle spinning (MAS) NMR spectra have been recorded on a Bruker Avance 300 NMR device operating at 7.04 T by the use of a 4 mm ZrO2 rotor. The resonance frequencies of the investigated nuclei are 44.167 MHz, 59.627 MHz and 121.495 MHz for ^{6}Li, ^{29}Si and ^{31}P, respectively. The rotational frequency was set to 8 kHz (^{29}Si), 12 kHz (^{31}P) and 15 kHz (^{6}Li and ^{31}P). The MAS NMR spectra have been acquired at room temperature with recycle delays from 10 s to 45 s and 200 to 1064 scans. All spectra regarding ^{6}Li were referenced to LiCl (1 M, aq) and LiCl (s) offering chemical shifts of 0.0 ppm and −1.15 ppm, respectively. Tetrakis(trimethylsilyl)silane was used as an external standard for the ^{29}Si spectra showing a chemical shift of −9.84 ppm referred to TMS. The ^{31}P spectra were referred to ammonium dihydrogen phosphate (s) with a chemical shift of 1.11 ppm regarding concentrated H_3PO_4. All spectra were recorded using single-pulse excitation.

Static ^{7}Li single pulse acquisition NMR experiments have been performed using a Bruker Avance III spectrometer operating at a magnetic field of 7.04 T employing a 4 mm WVT MAS probe. The resonance frequency of the measured ^{7}Li nucleus is 116.642 MHz. The sample has been sealed in a 4 mm glass tube to avoid contact with air and moisture. The temperature calibration for the measurements has been performed using the temperature-dependent ^{207}Pb NMR shift of lead nitrate as chemical shift thermometer, which has also been measured in a sealed glass tube. The static ^{7}Li NMR measurements were carried out in the temperature range from room temperature to 147 K with recycle delays from 1 s to 60 s and 4 scans. All spectra were referenced to LiCl (9.7 M, aq), for ^{7}Li.

Impedance Spectroscopy and DC Conductivity Measurements. The ionic conductivity of $Li_{14}SiP_6$ was determined by electrochemical impedance spectroscopy (EIS) in an in-house designed cell. The setup consists of two stainless-steel current collectors, a stainless-steel casing, a PEEK tube, hardened stainless-steel dies and pistons comprising a gasket for tightening the cell as well as six screws for fixing the cell (see Figure S12). Powdered samples of $Li_{14}SiP_6$ (510 mg) were placed between two 8 mm dies, and the screws were fastened with a torque of 30 Nm (corresponding to a theoretic pressure of 480 MPa), compressing the samples to 79% of the crystal density. For the determination of the compressed pellet thickness, six holes in a symmetric configuration were drilled into the current collectors, and the distance in between was measured using a precision caliper. Impedance spectra were recorded on a Bio-Logic potentiostat (SP-200) in a frequency range from 3 MHz to 50 mHz at a potentiostatic excitation of ±50 mV. Data were treated using the software EC-Lab (V 11.26). The measurements were performed in an Ar-filled glove box at 298 K. The electronic conductivity was determined with the same setup using a potentiostatic polarization applying voltages of 50, 100 and 150 mV for 16 h each. For the determination of the activation energy of the lithium ion conduction, the cell temperature

was set to 273, 298, 313, 333, and 353 K using a climate chamber (ESPEC, LU-114). The exact temperature profile is described in the Supporting Information as well as in Figure S13. Prior to EIS measurements, the cell rested 120 min to allow for thermal equilibration. EIS measurements were performed at both heating and cooling cycles. Temperature-dependent measurements were conducted outside the glove box, and the pistons were additionally greased to ensure a tight sealing of the cell from the ambient environment.

DFT Simulations. Density functional theory (DFT) total energy computations and DFT-based molecular dynamics (MD) simulations were carried out to complement the experimentally derived structures. Comparable DFT-MD techniques were recently used to study the related Li_2SiP_2 system.[32] Here, however, the presence of sites with fractional occupations make it necessary to construct a supercell model in which all atoms are located on discrete sites (Supporting Information). Such a supercell provides an approximant for the disordered structure but incurs substantial computational cost. Specifically, we used a 3×3×3 expansion of the conventional unit cell, ensuring an approximately isotropic distribution of Si atoms on the 8*c* position (such as to avoid close Si···Si contacts), and assessed different discrete occupation models for the Li-containing sites. Total-energy computations using CASTEP[33] confirmed that a full occupation of the position 8*c* and a vacancy formation on 4*b* is preferred over the alternative scenario of vacancy formation on 8*c* ("vacancy formation" here being equivalent to a fractional occupation of that site), by up to ≈ 10 kJ mol^{-1} in static computations (Figure S16), qualitatively corroborating the experimental refinement results. For the final 378-atom supercell model, high-temperature DFT-MD simulations were carried out using cp2k[34]. The system was gradually heated to 1300 K (30 ps), held at 1023 K (2.5 ps), followed by a production run at that temperature (5 ps), all with a timestep of 0.5 fs. Details of the protocol are provided as Supporting Information.

3. Results and Discussion

Syntheses and Structure of $Li_{14}SiP_6$. For the search of novel Li-rich compositions we investigated stoichiometric ratios along the line connecting Li_3P and Li_8SiP_4 in the Li-Si-P Gibbs triangle (Figure 1). Extrapolation of this sequence to higher amounts of lithium by the formal addition of "Li_3P" units results in the nominal compositions "$Li_{11}SiP_5$", "$Li_{14}SiP_6$", "$Li_{17}SiP_7$", and "$Li_{20}SiP_8$". Materials of these compositions were prepared applying a recently described preparative route for phosphidotetrelates starting from mechanical alloying of the elements in the stoichiometric amounts, followed by a high-temperature reaction of the mixtures in sealed, carbon-coated silica glass ampoules.[19] After the mechanical alloying process, PXRD data reveal the initial formation of a cubic antifluorite structure type. However, the extremely broadened reflections indicate small crystal sizes. Additionally, at that stage an intense and broad x-ray amorphous halo implies the presence of large amounts of glassy phases. The microcrystalline, single-phase $Li_{14}SiP_6$ is obtained by quenching the hot ampoule with the ball-milled product in water after 6-18 h of annealing at 973 K. Variation of annealing time within that frame does not lead to detectable differences in the crystal structure or sample purity. Simultaneous refinement of powder Mo X-ray and neutron diffraction shows a high agreement of the two methods and confirms the structure model (Figure 2). Details of the Rietveld refinements are shown in Table 1.

Experiments with the nominal stoichiometry of "$Li_{11}SiP_5$" in analogy to $Li_{14}SiP_6$ reveal a mixture of $Li_{14}SiP_6$ and Li_8SiP_4[18], whereas investigations of compositions with a higher amount of lithium and phosphorus ("$Li_{17}SiP_7$" and "$Li_{20}SiP_8$") lead to a mixture of $Li_{14}SiP_6$ and Li_3P (Figure S3 in the Supporting Information). According to these results $Li_{14}SiP_6$ is assumed to be the lithium-richest compound on the quasi-binary line between Li_3P and "Si_3P_4". Moreover, no significant phase width according to "$Li_{14-4x}Si_{1+x}P_6$" is found at the Li_3P-rich side, while at the Li_3P-poor side a Si-enriched composition "$Li_{14-4x}Si_{1+x}P_6$" seems to exist (Supporting Information).

The lithium-rich compound $Li_{14}SiP_6$ crystallizes in the Li_3Bi structure type[35] with the cubic space group $Fm\bar{3}m$ (no. 225) and a lattice parameter of 5.91566(6) Å at 4 K (Figure 3). The crystal structure was determined from the data of a single crystal X-ray diffraction measurement at 123 K, of temperature-dependent powder neutron diffraction measurements between 4 K and 1023 K and from a simultaneous refinement of powder neutron and X-ray diffraction patterns obtained at 300 K. Atomic coordinates and anisotropic displacement parameters as well as the results from the powder neutron diffraction measurement at 4 K and from the single crystal X-ray diffraction at 123 K are given in the Supporting Information.

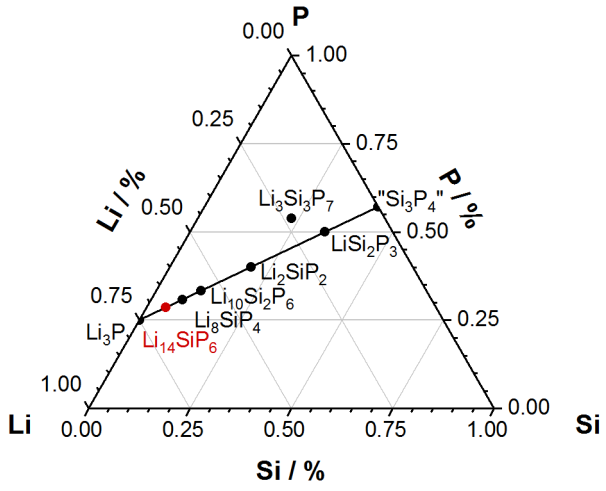

Figure 1. Gibbs triangle of the ternary Li-Si-P composition diagram with formulae of known compounds. The new compound $Li_{14}SiP_6$ is highlighted in red.

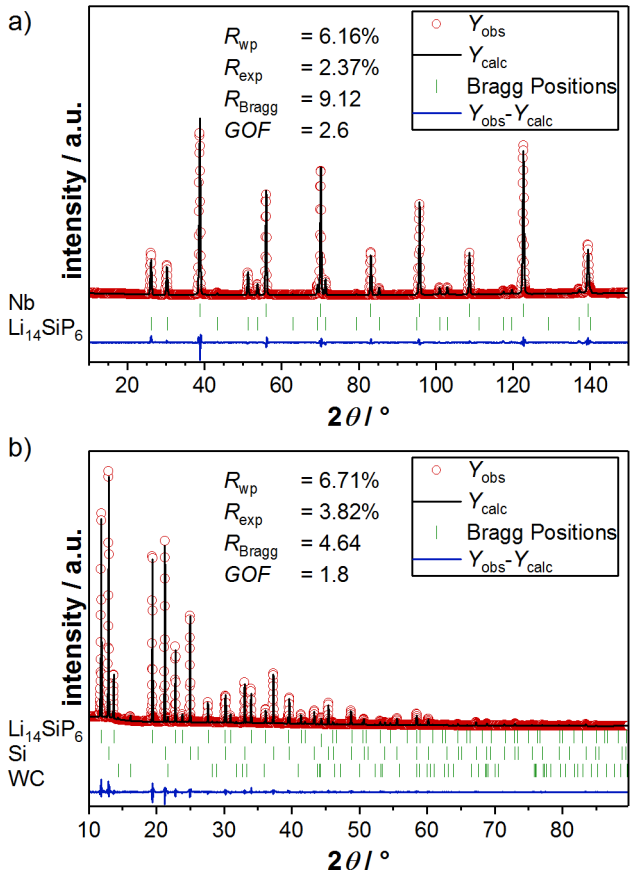

Figure 2. Results from the joint Rietveld refinement of $Li_{14}SiP_6$. a) Rietveld analysis of the powder neutron diffraction pattern (λ = 1.5482 Å) of $Li_{14}SiP_6$ at 300 K. b) Rietveld analysis of the powder X-ray diffraction pattern (λ = Mo $K_{\alpha1}$) of $Li_{14}SiP_6$ at 300 K. In both diffraction patterns red circles indicate observed intensities Y_{obs}, black lines show calculated intensities Y_{calc}, blue lines reveal the difference between observed and calculated intensities, and green marks indicate Bragg positions of $Li_{14}SiP_6$ and Nb (ampoule) or $Li_{14}SiP_6$, Si (added as internal standard to the PXRD sample) and WC (abrasion), respectively.

Table 1. Details of the joint Rietveld structure refinement of $Li_{14}SiP_6$ from neutron and X-ray diffraction measurements at 300 K

empirical formula	$Li_{2.33}Si_{0.17}P$ (neutron diffr.)	$Li_{2.33}Si_{0.17}P$ (X-ray diffr.)
T / K	300	
formula weight / g mol^{-1}	51.86	
space group (no.)	$Fm\bar{3}m$ (225)	
unit cell parameters / Å	a = 5.93927(1)	
Z	4	
V / Å^3	209.507(1)	
$\rho_{calc.}$ / g cm^{-3}	1.644	
diffracted beam	neutrons	X-rays
λ / Å	1.5482	0.70926
2θ range / deg	9.0000-151.89999	10.0000-89.78600
R_p	4.62%	4.79%
R_{wp}	6.16%	6.71%
R_{exp}	2.37%	3.82%
X^2	6.73	3.07
GOF	2.6	1.8
R_{Bragg}	9.12	4.64
R_f	5.79	14.8
depository no.	CSD-1915806	CSD-1915824

The unit cell of $Li_{14}SiP_6$ contains three crystallographic atom positions (P1, Li1/Si1 and Li2). The structure is closely related to the antifluorite type of structure, as it is based on a cubic close packing (*ccp*) of P atoms on the 4*a* site, with all tetrahedral voids (8*c* site) fully occupied by Li1 and Si1 atoms in a mixed occupancy ratio of 11:1. Additionally, all octahedral voids (4*b* site) are occupied by Li atoms (Li2) with a probability of 50%. All interatomic Si-P distances (2.5616(1) Å; due to symmetry identical: Li1-P, Li2-Si, Li1-Li2), Li2-P (2.96964(1) Å) and P-P distances (4.19970(1) Å) are within the range of those found for related ternary or binary compounds like Li_8SiP_4[18], Li_2SiP_2,[18,25] $LiSi_2P_3$,[25] $Li_{10}Si_2P_6$[24], Li_3P[36], and $Li_{17}Si_4$[37]. As a consequence of the occupational disorder of Li1 and Si1, the structure contains $[SiP_4]^{8-}$ tetrahedra (ortho-phosphidosilicate) and P^{3-} ions in a ratio of 1:2; the negative charge is compensated by 14 lithium ions located in close vicinity.

Despite the structural similarity of $Li_{14}SiP_6$ to the Li_3Bi-strcuture type the compositionally related compound Li_3P crystallizes in a different structure type (space group: $P6_3/mmc$). Whereas $Li_{14}SiP_6$ derives from a *ccp* of P atoms, Li_3P can be derived from a hexagonal close packing of P atoms. In this structure the tetrahedral voids and the trigonal faces shared by octahedral voids are occupied with Li. In $Li_{14}SiP_6$, Li also fills tetrahedral voids, but is additionally centered in octahedral voids. The variances in the structure suggests a stabilization of the cubic phase by the introduction of Si atoms that covalently bind to four P atoms. Due to the conservation of charge balance, the incorporation of Si (or formal Si^{4+}) reduces the amount of Li^+ by a factor of four, which in consequence leads to a partially filled Li position (8*c* site).

In $Li_{14}SiP_6$, the presence of isolated tetrahedral SiP_4 anions is confirmed by the ^{29}Si MAS NMR spectrum showing one distinct resonance at 10.4 ppm (Figure S8 in the Supporting Information) which is rather close to the value of 11.5 ppm observed for discrete $[SiP_4]^{8-}$ tetrahedra in Li_8SiP_4, whereas the signals of covalently connected tetrahedra occur in the range from −3.3 to −14.8 ppm as observed for Li_2SiP_2 and $Li_3Si_3P_7$.[18, 24]

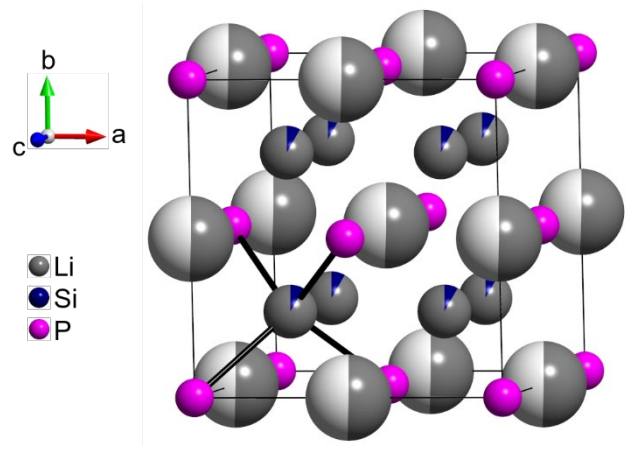

Figure 3. Structure of $Li_{14}SiP_6$ at 4 K. P atoms, mixed Li/Si sites and partially occupied Li sites are depicted as pink, grey/indigo and grey/white displacement ellipsoids, respectively, set at 90% probability. Black lines mark (Li/Si)-P bonds resulting in $(Li/Si)P_4$ tetrahedra.

Although the crystal structure contains only one crystallographic P site, two broad, distinct signals are detected in the ^{31}P MAS NMR spectra at −226.9 and −316.8 ppm (12 kHz, Figure S9 in the Supporting Information). In spite of the disorder of Li and Si, the P atoms are situated in different chemical environments – either surrounded by eight Li atoms or by one Si atom and seven Li atoms in the neighboring tetrahedral voids – and by a different number of atoms in the six, partially filled octahedral voids. These considerably different chemical environments lead to a strong broadening of the signals.[38] As observed in the ^{31}P MAS NMR spectra of related compounds,[18, 24] a covalent Si-P bond has a significant effect on the chemical shift: the lower the number of neighboring Si atoms and thus the higher the negative partial charge of the P atom is, the stronger is the upfield shift of the signal. Consequently, the signal at −226.9 ppm can be assigned to the terminal phosphorus atoms in the covalently bound $[SiP_4]^{8-}$ units that matches well the characteristic range of terminal phosphorus atoms of $[SiP_4]^{8-}$ tetrahedra in Li_8SiP_4[18] and $Li_{10}Si_2P_6$,[24] whereas the signal at −316.8 ppm is assigned to the isolated P^{3-} units without covalent bonds and surrounded by eight lithium ions in a cubic arrangement.

According to the ratio of one $[SiP_4]^{8-}$ tetrahedron containing four P atoms and two P^{3-} anions, the ratio of the total integrated intensity of the two ^{31}P NMR signals should be 2:1. The slightly higher experimental ratio of 2.3:1 (12 kHz) results either from an overlap of the signals with the spinning sidebands of the respective adjacent signals, as their accessible spinning frequencies are in the range of the chemical shift difference of the two signals, or it indicates the additional presence of bridging P atoms between edge- or corner-sharing SiP_4 tetrahedra. Such bridging P atoms might cause a larger shift between −120 and −240 ppm,[18,24,38] which could overlap with the signals of terminal P atoms. However, the probability of a subsequent occupation of neighboring tetrahedral voids by Si atoms leading to sharing corners or edges of SiP_4 tetrahedra, should be rather small, owing to the electrostatic repulsion of the formally fourfold positively charged Si atoms.

As known from all other lithium phosphidosilicates the ^6Li MAS NMR spectrum of $Li_{14}SiP_6$ shows only one signal at 5.4 ppm (Figure S7 in the Supporting Information).[18,24-25]

Thermal Properties of $Li_{14}SiP_6$. In order to apply the maximum entropy method at 1023 K, $Li_{14}SiP_6$ was studied by temperature-dependent powder neutron diffraction experiments. Within the investigated temperature range from 4 to 1023 K, the unit cell parameter increases from 5.9158(1) to 6.0785(3) Å in the lower temperature range. Between 623 and 673 K $Li_{14}SiP_6$ decomposes entirely, indicating a fast transition. The phase mixture is thermodynamically stable up to temperatures between 873 and 923 K. The lithium-rich phase $Li_{14}SiP_6$ reappears at 923 K with a proportion of about 80% and is completely converted at 973 K (Figure 4). During these transition processes all Bragg reflections of the involved compounds remain distinct with narrow line widths, suggesting the formation of large crystal domains. The transition temperatures are confirmed by differential scanning calorimetry (DSC) of $Li_{14}SiP_6$ and the corresponding evaluation is given as Supporting Information.

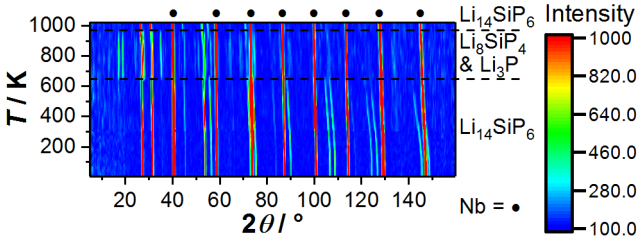

Figure 4. 2D plot of the data of temperature-dependent neutron diffraction measurements from 4 to 1023 K in a 2θ range from 5 to 160° (sample sealed under Ar). With increasing temperature $Li_{14}SiP_6$ decomposes into Li_8SiP_4 and Li_3P, and is reformed again. The ampoule material Nb is indicated with solid circles.

The supplementary evaluation of the executed Rietveld refinements from temperature-dependent neutron diffraction experiments exhibited a nonlinear increase of the lattice parameters of $Li_{14}SiP_6$ upon heating (Figure 5). Furthermore, the quasi-linear trend of increasing lattice parameters observed prior to the phase transition is continued at 973 and 1023 K, indicating a complete recovery of the initial structure obtained via quenching. The lattice dimension of Li_8SiP_4, as normalized to formula units, has been found systematically smaller and is characterized by a lower thermal expansion rate than that of $Li_{14}SiP_6$.

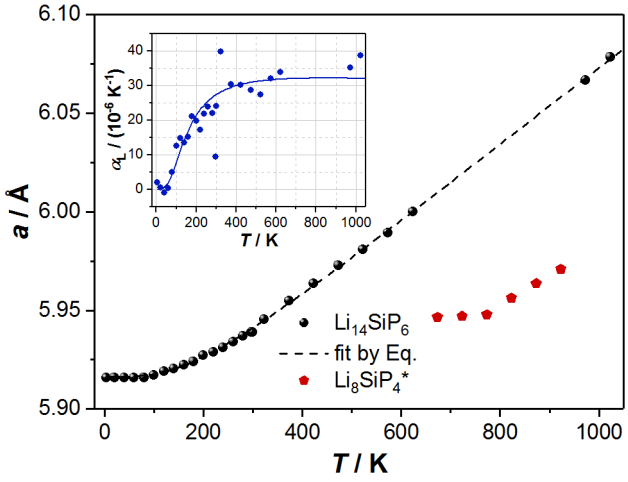

Figure 5. Thermal-dependence of the lattice parameters a and of the thermal expansion coefficient (calculated as $\alpha_l(T) = \partial \ln l(T)/\partial T$) (inset) of the $Li_{14}SiP_6$ sample upon heating

under Ar. The normalized $a/2$ lattice parameters for the intermediate phase Li_8SiP_4 are shown by red points.

Similar to other thermodynamic quantities the temperature evolution of the lattice dimensions, and, correspondingly, the thermal expansion can be modeled. As it has been shown in previous studies[39-41] the thermal dependency of the lattice parameter can be modeled by means of the first order Grüneisen approximation

$$V(T)=(a(T))^3=V_0+\frac{\gamma}{K_T}U(T)$$
$$=V_0+\frac{\gamma}{K_T}\left[9Nk_BT\left(\frac{T}{\theta_D}\right)^3\int_0^{\theta_D/T}\frac{x^3}{e^x-1}dx\right] \quad (1)$$

where V_0 denotes the hypothetical cell volume at zero temperature, γ is the Grüneisen constant, K_T is the bulk modulus, and U is the internal energy of the system. Both γ and K_T are assumed to be temperature independent, and the use of the Debye approximation for the internal energy U in Eq. 1 with the characteristic temperature θ_D usually provides a reasonable description.

The least-square minimization fit of the experimental temperature dependence of cell volumes by Eq. 1 yields 207.093 ± 0.066 Å^3, 2507 · 10^{-14} ± 37 · 10^{-14} Pa^{-1} and 659 ± 31 K for V_0, the γ/K_T ratio and θ_D, respectively. The fit was characterized by a high coefficient of determination 0.999965, and the graphical results are shown in Figure 5 by dashed lines.

The linear thermal expansion coefficient was calculated from the thermal evolution of the lattice parameter via $\alpha_l(T)=\partial\ln l(T)/\partial T$, and the result is shown in the inset of Figure 5. The thermal expansion of $Li_{14}SiP_6$ grows upon heating from 0 K to ca. 27.5 · 10^{-6} K^{-1} and becomes almost temperature independent α_l = 32 · 10^{-6} K^{-1} above 500 K, which is corresponding to ca. 0.8 θ_D, indicating a quasi-classical behavior of $Li_{14}SiP_6$ at these temperatures.

Lithium Ion Mobility. The dynamic behavior of the lithium ions was investigated via the temperature-dependent evolution of the static ^{7}Li NMR line width in the relevant temperature range. Since the central transition of the I = 3/2 nucleus ^{7}Li is only broadened by the homo- (^{7}Li-^{7}Li) and heteronuclear (here: ^{7}Li-^{31}P) dipolar couplings, and both types of interactions scale with the second Legendrian ($3\cos^2\beta$-1), any dynamic process should produce a (partial) averaging of the orientational dependence and hence entail a narrowing of the NMR line.

The temperature-dependent evolution of the ^{7}Li NMR spectra is shown in Figure 6a. Only one Lorentzian-shaped signal at 4.8 ppm is visible at room temperature with a linewidth of 523 Hz. Upon cooling of the $Li_{14}SiP_6$ sample, this signal gradually broadens and develops a Gaussian lineshape with a linewidth of 10.2 kHz at 147 K. Figure 6b shows the temperature-dependent evolution of the linewidth (FWHH) of the static ^{7}Li-onepulse measurements. A rough estimation of the activation energy can be done by the empirical Waugh-Fedin relation, E_A^{NMR} = 0.156 · T_{onset}. The onset temperature was determined to 190 K which leads to an activation energy of 30 kJ mol^{-1} (~ 0.31 eV).

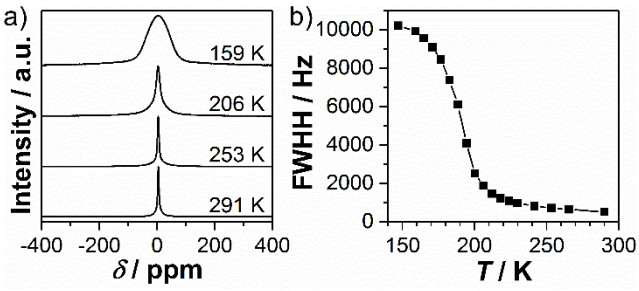

Figure 6. a) ^{7}Li NMR spectra of $Li_{14}SiP_6$ recorded at different temperatures. b) Evolution of the temperature-dependent ^{7}Li-linewidths of $Li_{14}SiP_6$. Solid line serves only as a guide to the eye.

In addition, the lithium ion conductivity of $Li_{14}SiP_6$ was determined from impedance measurements in a blocking electrode configuration. Impedance spectra at different temperatures (273, 298, 313, 333, and 353 K, according to the temperature profile shown in the inset) are displayed in Figure 7a, featuring a semi-circle at high frequencies and a low frequency tail. The semi-circle can be described as parallel circuit element of a resistor and a constant phase element (R/Q), with R representing both intragrain and grain boundary contributions to the lithium ion transport, which could not be resolved, and thus only the total ionic resistance of the sample could be determined. The fitted α values (> 0.98) of the constant phase elements are reasonable close to 1, hence, the constant phase exponent was neglected, in which case the Q parameter becomes essentially equivalent to a capacitance, with a value of ≈ 4.2 · 10^{-10} F for 298 K. This value lies in between the typical range for intragrain (≈ 10^{-12} F) and grain boundary (≈ 10^{-9} F) capacitances.[42] The ionic conductivity was determined to $\sigma_{Li}(Li_{14}SiP_6)$ = (1.09 ± 0.06) · 10^{-3} S cm^{-1} at 298 K (obtained from three independently measured cells). The activation energy for lithium ion transport (Figure 7b) is investigated by temperature-dependent impedance measurements in a range from 273 to 353 K, yielding an E_A^{PEIS} of 32.2 ± 0.6 kJ mol^{-1} (~ 0.33 eV); this was determined from three independently measured cells, using the $\sigma_{Li} \cdot T$ values of only the first heating and cooling cycle of each sample. The temperature ramp of a heating and cooling cycle is displayed in the inset of Figure 7a. Colored dots indicate at which temperatures PEIS measurements were performed. In this context it shall be mentioned that conductivities (and thus the product of $\sigma_{Li} \cdot T$) for heating and cooling differ by less than 5% at 298 and 333 K, whereas at 313 K the $\sigma_{Li} \cdot T$ values obtained in the cooling branch are clearly higher than those obtained in the heating branch (by ≈ 58%), although the cell was in thermal equilibrium. This hysteresis was reproducibly observed for all measured cells of this compound (three independently built and measured cells) and hence is no artifact, but rather must be a compound related phenomenon. The exact reason for the observed hysteresis is still under investigation. Error bars are calculated separately for heating and cooling steps by taking the mean of three independent measurements. DC polarization measurements in the range from 50 to 150 mV reveal an electronic conductivity of (1.64 ± 0.04) · 10^{-7} S cm^{-1} at 298 K (based on the standard deviation of three cells).

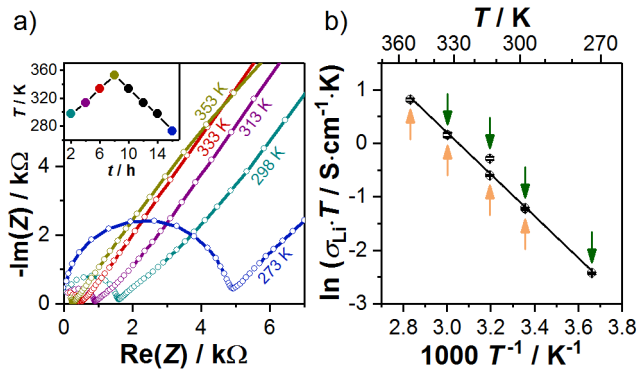

Figure 7. a) Nyquist plot of $Li_{14}SiP_6$ measured under blocking conditions, with spectra recorded at temperatures between 273 and 353 K during a heating cycle, according to color coding of the inset which shows the temperature profile of a cycle for these temperature dependent measurements. Colored dots indicate the temperatures at which impedance was measured. b) Arrhenius plot of the product of conductivity and temperature ($\sigma_{Li} \cdot T$) obtained in the heating as well as in the cooling branch, with error bars for each based on the standard deviation from independent measurements with three cells; the shown linear fit through both branches was used to obtain the activation energy E_A^{PEIS}. Since the differences of the average ($\sigma_{Li} \cdot T$) values obtained during heating vs cooling are very small, they are marked by the orange and green arrows, respectively.

Lithium Diffusion Pathways in $Li_{14}SiP_6$. In $Li_{14}SiP_6$ only lithium (in its natural isotope composition) possesses a negative scattering length ($b_{Li} = -1.9$ fm). This is very beneficial, since the study of experimental lithium diffusion pathways may be limited to the analysis of the distribution of negative components in nuclear density maps. Accurate nuclear density maps were extracted from the experimental structure factors and phases measured at 1023 K by the maximum entropy method (MEM). This method in general is based on the estimation of 3D scattering densities from a limited amount of information by maximizing information entropy under restraints, consistent with experimental observations.[43] Compared to Fourier analysis the MEM often delivers more accurate electron/nuclear density maps from powder diffraction datasets having "limited" statistics, i.e. termination effects and artefacts of various kinds often occur to be less pronounced in MEM evaluations.

Negative nuclear density maps for $Li_{14}SiP_6$ reconstructed from experimental structure factors using the program Dysnomia[44] are plotted in Figure 8. The MEM analysis of the nuclear densities yields 3D lithium diffusion pathways in $Li_{14}SiP_6$ involving both of the lithium sites 4*b* and 8*c*. Large sphere-like volumes on negative nuclear density maps correspond to the lithium location and are connected by well-resolved necks, which define the energy barrier for lithium diffusion in $Li_{14}SiP_6$. As illustrated, it is obvious that there is a connection between face-sharing tetrahedral and octahedral voids. Thus, neither lithium diffusion via edge-sharing tetrahedral voids nor a lithium ion hopping mechanism between edge-sharing octahedral voids could be ascertained for $Li_{14}SiP_6$. The latter is also hindered by the large interatomic distances of the adjacent Li2 atoms centered in the octahedral voids (4*b*).

The lithium motion, which is visualized in Figure 9a, occurs from the 8*c* site (Li1) to a vacancy on the 4*b* site. Interestingly the diffusion does not occur along the direct connection (shortest distance) between the two adjacent sites 8*c* and 4*b*, but proceeds via a well-defined neck (i.e. ●) with the lattice coordinates of 96*k* (0.40276 | 0.59724 | 0.305) and ..*m* site symmetry.

Assuming a quasi-classical behavior of $Li_{14}SiP_6$ at temperatures above 500 K, the experimental nuclear/probability densities can be analyzed in the form of an activation energy landscape. Since the lithium is the only negative scatterer in $Li_{14}SiP_6$ the one-particle potential (OPP) for lithium was recalculated from negative nuclear densities. Its 2D distribution in the (110, d = 1.0) plane is shown in Figure 9b. The direct Li1-Li2 pathway is characterized by an activation barrier larger than 1.4 eV (~ 135 kJ mol^{-1}) at 32*f* (0.36 | 0.64 | 0.36). A sufficiently lower activation barrier of 0.44 eV (~ 42 kJ mol^{-1}) occurs along the pathway involving the previously mentioned neck at 96*k*, i.e. Li1-●-Li2. The small activation barrier at the Li2 site is considered as an artefact of the data evaluation.

While it is not feasible for DFT simulations to map out all atomistic diffusion pathways in the system, due to the presence of disorder (which formally makes all pathways inequivalent, and requires a supercell approximant; Methods section), we did perform DFT-based MD simulations at high temperature that qualitatively corroborate the mechanism for lithium diffusion in the title compound. At a simulation temperature around that of the MEM analysis (1023 K), the Li atoms are seen to be highly mobile and frequently change positions (Figure 10a-b); several instances of Li atom motion across the 8*c* and 4*b* sites were observed in the DFT-MD trajectory. On the other hand, the heavier Si and P atoms show thermal vibrations but the *ccp*-like anion sublattice and the $[SiP_4]^{8-}$ units remained intact otherwise during our simulation, providing further evidence for the validity of the structural model (Figure 10c). At such high temperature, the structure could be viewed as a framework of isolated $[SiP_4]^{8-}$ and P^{3-} units between which the Li atoms are readily moving in all directions, consistent with the experimentally observed Li mobility even at much lower temperature.

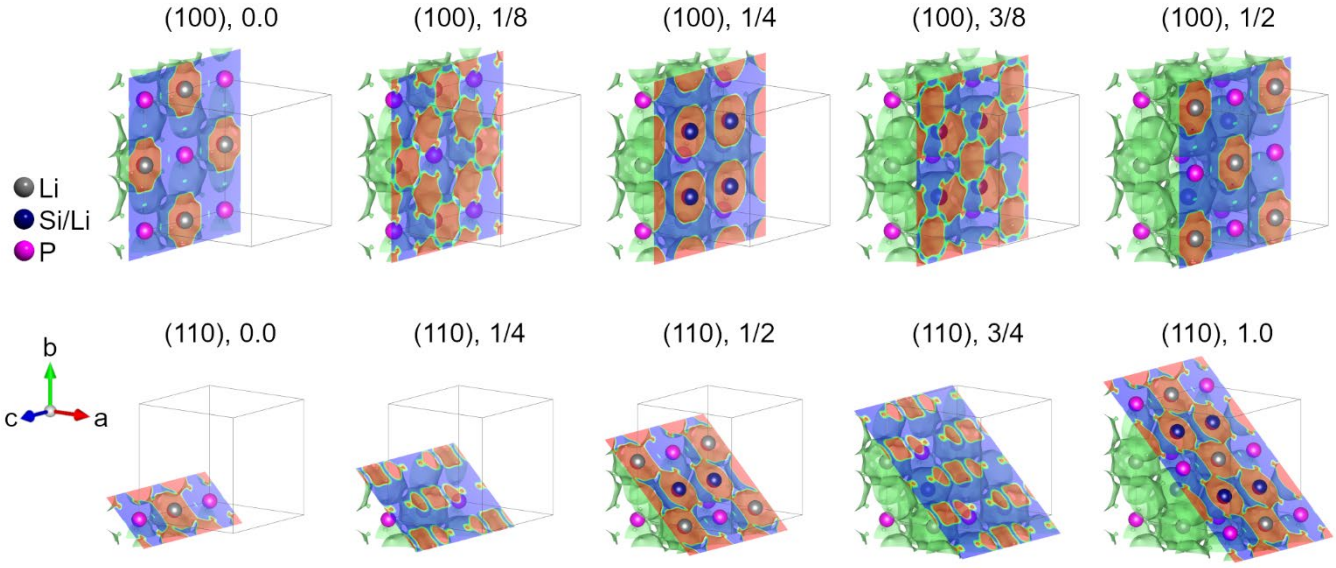

Figure 8. Negative nuclear density distribution in $Li_{14}SiP_6$ reconstructed from experimental structure factors at 1023 K using the maximum entropy method (surface threshold −0.01 fm/Å^3, cell grid 256×256×256) for various lattice planes defined by Miller indices (h, k, l) and number of position. Li, P and mixed Li/Si sites are shown as grey, pink and dark blue spheres, respectively.

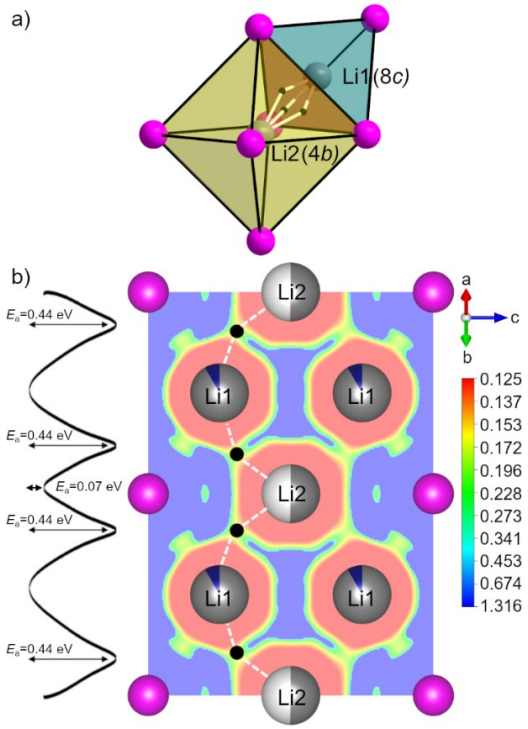

Figure 9. a) Sketch of diffusion pathways in $Li_{14}SiP_6$ between face-sharing tetrahedral (8*c*) and octahedral voids (4*b*) indicated by white lines going straight through the neck ● at the general position (0.40276 | 0.59724 | 0.305). Li and P are shown as grey and pink spheres, respectively. b) The 2D section cut (110, d = 1 plane) of the lithium one-particle-potential (OPP, red ≙ low, blue ≙ high) and its 1D section along dashed lines connecting five Li atoms in a chain Li2-●-Li1-●-Li2-●-Li1-●-Li2, where ● corresponds to the neck connecting neighboring sites with partial Li occupations. Li, P and mixed Li/Si sites are shown as grey, pink and dark blue spheres, respectively.

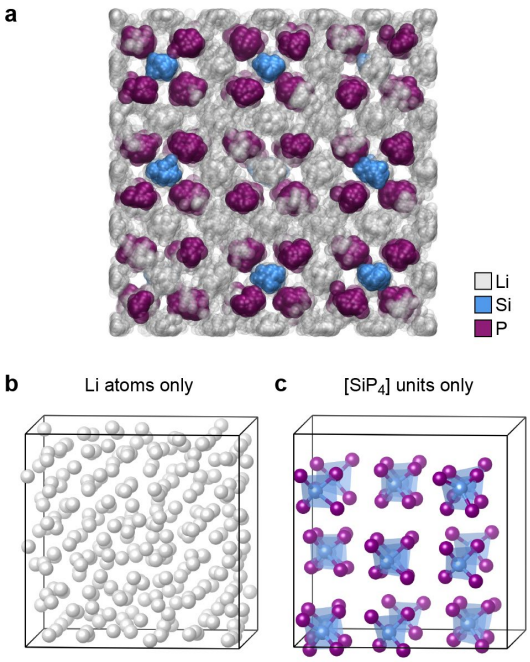

Figure 10. DFT-MD modeling of Li^+ dynamics in $Li_{14}SiP_6$. a) Snapshots from a trajectory at around 1023 K, showing atoms as partially translucent spheres (Li/Si, smaller; P, larger) and overlaying 100 equidistant images to provide an impression of the atomic mobility. The cell has been shifted by (*a*/4, *a*/4, 0) to ease visualization. b) Final image of the simulation, showing the Li atoms only, and indicating the boundaries of the simulation cell by a thin line. c) Same but showing only the Si atoms and the P atoms in their direct vicinity; the tetrahedral $[SiP_4]^{8-}$ units remain intact during the simulation, as emphasized by shading. Structures were visualized using VMD[45] and VESTA[29]. Details of the supercell model construction are provided as Supporting Information.

4. Conclusion

The so far lithium-richest phosphidosilicate $Li_{14}SiP_6$ crystallizes in the highly symmetric space group $Fm\bar{3}m$ (no. 225). The

compound combines structural simplicity with P atoms forming a simple *ccp* atom arrangement with an intriguing degree of complexity, specifically mixed occupations and high mobility of Li atoms. The formation of a cubic structure starts already during the mechanical milling process, as the powder X-ray diffraction experiments reveal the corresponding admittedly broadened but evident reflection pattern, and is finished upon a heat treatment at 973 K. DSC analyses and temperature-dependent neutron diffraction experiments revealed a remarkable thermal behavior of the novel compound. $Li_{14}SiP_6$ is a high-temperature phase and decomposes at temperatures below 973 K into Li_8SiP_4 and Li_3P. The decomposition and reformation proceeds within a distinct temperature range and, therefore, in order to obtain pure $Li_{14}SiP_6$ rapid cooling of the samples after the heat treatment is essential. Structural analysis combining both neutron and X-ray diffraction methods as well as static and MAS solid-state NMR spectroscopy exhibited a disorder of Si and Li atoms within the tetrahedral voids of the *ccp* of P atoms. An investigation of the negative nuclear density distribution via MEM affords a clearer understanding of the lithium ion motion within the crystal structure. The data show that the 3D lithium ion diffusion involves both 4*b* and 8*c* lithium sites, and that it occurs preferably between face-sharing tetrahedral and octahedral voids. The material shows an ionic conductivity of about $1.1 \cdot 10^{-3}$ S cm^{-1} at 298 K, an electronic conductivity of $1.6 \cdot 10^{-7}$ S cm^{-1} at 298 K and an activation energy of 30-32 kJ mol^{-1}. Hence, compared to the related compound Li_8SiP_4, the incorporation of supplementary lithium ions as well as the structural change and the occurring cation disorder within the structure result in considerably increased ionic conductivity, higher mobility and lower activation energy.[18-19]

Since the first report of Li ion conductivity in lithium phosphidotetrelates,[18] the ionic conductivity in $Li_{14}SiP_6$ reported here marks an increase over two orders of magnitude in this system within three years. With only a moderate number of known examples in hands, the reported conductivities almost match those of well-established crystalline lithium ion conductors[16], and a further enhancement of the ionic transport via manipulation by chemical, electronic and structural means is anticipated. Further investigations on the electrochemical stability and performance of $Li_{14}SiP_6$ and future, related materials are necessary to provide information, if this material class is conceivable for application in all-solid-state batteries.

ASSOCIATED CONTENT

Supporting Information. Details of the crystal structure determination, Coordination polyhedra, Phase width analysis, Differential scanning calorimetry (DSC), ^{6}Li, ^{29}Si and ^{31}P MAS NMR spectroscopy, Electrochemical impedance spectroscopy (EIS), DFT simulations.

This material is available free of charge via the Internet at http://pubs.acs.org."

AUTHOR INFORMATION

Corresponding Author

*E-mail: Thomas.faessler @lrz.tu-muenchen.de.

Author Contributions

The manuscript was written through contributions of all authors. / All authors have given approval to the final version of the manuscript. / ‡ S.S. and H.E.: These authors contributed equally to this work.

Funding Sources

The work was carried out as part of the research project ASSB coordinated by ZAE Bayern. The project is funded by the Bavarian Ministry of Economic Affairs, Regional Development and Energy. Volker L. Deringer acknowledges a Leverhulme Early Career Fellowship and support from the Isaac Newton Trust. This work used the ARCHER UK National Supercomputing Service via EPSRC Grant EP/P022596/1.

Notes

No additional relevant notes.

ACKNOWLEDGMENT

The authors greatly acknowledge Tassilo Restle for DSC measurements, and Johannes Landesfeind and Tanja Zünd for the design of the conductivity measurement cell.

REFERENCES

(1) Janek, J.; Zeier, W. G. A Solid Future for Battery Development. *Nat. Energy* **2016**, *1*, 16141.

(2) Kireeva, N.; Pervov, V. S. Materials Space of Solid-State Electrolytes: Unraveling Chemical Composition-Structure-Ionic Conductivity Relationships in Garnet-Type Metal Oxides Using Cheminformatics Virtual Screening Approaches. *Phys. Chem. Chem. Phys.* **2017**, *19*, 20904-20918.

(3) Richards, W. D.; Miara, L. J.; Wang, Y.; Kim, J. C.; Ceder, G. Interface Stability in Solid-State Batteries. *Chem. Mater.* **2016**, *28*, 266-273.

(4) West, A. R., *Solid State Chemistry and its Applications*. 2nd Ed., Student Ed.; John Wiley & Sons, Ltd: West Sussex, United Kingdom, 2014.

(5) Zeier, W. G.; Zhou, S.; Lopez-Bermudez, B.; Page, K.; Melot, B. C. Dependence of the Li-Ion Conductivity and Activation Energies on the Crystal Structure and Ionic Radii in $Li_6MLa_2Ta_2O_{12}$. *ACS Appl. Mater. Interfaces* **2014**, *6*, 10900-10907.

(6) Kraft, M. A.; Culver, S. P.; Calderon, M.; Böcher, F.; Krauskopf, T.; Senyshyn, A.; Dietrich, C.; Zevalkink, A.; Janek, J.; Zeier, W. G. Influence of Lattice Polarizability on the Ionic Conductivity in the Lithium Superionic Argyrodites Li_6PS_5X (X = Cl, Br, I). *J. Am. Chem. Soc.* **2017**, *139*, 10909-10918.

(7) Kanno, R.; Hata, T.; Kawamoto, Y.; Irie, M. Synthesis of a New Lithium Ionic Conductor, thio-LISICON–Lithium Germanium Sulfide System. *Solid State Ionics* **2000**, *130*, 97-104.

(8) Murayama, M.; Kanno, R.; Irie, M.; Ito, S.; Hata, T.; Sonoyama, N.; Kawamoto, Y. Synthesis of New Lithium Ionic Conductor thio-LISICON—Lithium Silicon Sulfides System. *J. Solid State Chem.* **2002**, *168*, 140-148.

(9) Murayama, M.; Kanno, R.; Kawamoto, Y.; Kamiyama, T. Structure of the thio-LISICON, Li_4GeS_4. *Solid State Ionics* **2002**, *154–155*, 789-794.

(10) Deiseroth, H.-J.; Kong, S.-T.; Eckert, H.; Vannahme, J.; Reiner, C.; Zaiß, T.; Schlosser, M. Li_6PS_5X: A Class of Crystalline Li-Rich Solids with an Unusually High Li^+ Mobility. *Angew. Chem., Int. Ed.* **2008**, *47*, 755-758.

(11) Kamaya, N.; Homma, K.; Yamakawa, Y.; Hirayama, M.; Kanno, R.; Yonemura, M.; Kamiyama, T.; Kato, Y.; Hama, S.; Kawamoto, K.; Mitsui, A. A Lithium Superionic Conductor. *Nat. Mater.* **2011**, *10*, 682-686.

(12) Bron, P.; Johansson, S.; Zick, K.; Schmedt auf der Günne, J.; Dehnen, S.; Roling, B. $Li_{10}SnP_2S_{12}$: An Affordable Lithium Superionic Conductor. *J. Am. Chem. Soc.* **2013**, *135*, 15694-15697.

(13) Kuhn, A.; Gerbig, O.; Zhu, C.; Falkenberg, F.; Maier, J.; Lotsch, B. V. A New Ultrafast Superionic Li-Conductor: Ion Dynamics in $Li_{11}Si_2PS_{12}$ and Comparison with other Tetragonal LGPS-Type Electrolytes. *Phys. Chem. Chem. Phys.* **2014**, *16*, 14669-14674.

(14) Kato, Y.; Hori, S.; Saito, T.; Suzuki, K.; Hirayama, M.; Mitsui, A.; Yonemura, M.; Iba, H.; Kanno, R. High-Power All-Solid-State Batteries Using Sulfide Superionic Conductors. *Nat. Energy* **2016**, *1*, 16030.

(15) Wang, B.; Chakoumakos, B. C.; Sales, B. C.; Kwak, B. S.; Bates, J. B. Synthesis, Crystal Structure, and Ionic Conductivity of a Polycrystalline Lithium Phosphorus Oxynitride with the γ-Li_3PO_4 Structure. *J. Solid State Chem.* **1995**, *115*, 313-323.

(16) Bachman, J. C.; Muy, S.; Grimaud, A.; Chang, H.-H.; Pour, N.; Lux, S. F.; Paschos, O.; Maglia, F.; Lupart, S.; Lamp, P.; Giordano, L.; Shao-Horn, Y. Inorganic Solid-State Electrolytes for Lithium Batteries: Mechanisms and Properties Governing Ion Conduction. *Chem. Rev.* **2016**, *116*, 140-162.

(17) Juza, R.; Schulz, W. Ternäre Phosphide und Arsenide des Lithiums mit Elementen der 3. und 4. Gruppe. *Z. Anorg. Allg. Chem.* **1954**, *275*, 65-78.

(18) Toffoletti, L.; Kirchhain, H.; Landesfeind, J.; Klein, W.; van Wüllen, L.; Gasteiger, H. A.; Fässler, T. F. Lithium Ion Mobility in Lithium Phosphidosilicates: Crystal Structure, ^{7}Li, ^{29}Si, and ^{31}P MAS NMR Spectroscopy, and Impedance Spectroscopy of Li_8SiP_4 and Li_2SiP_2. *Chem. Eur. J.* **2016**, *22*, 17635-17645.

(19) Eickhoff, H.; Strangmüller, S.; Klein, W.; Kirchhain, H.; Dietrich, C.; Zeier, W. G.; van Wüllen, L.; Fässler, T. F. Lithium Phosphidogermanates α- and β-Li_8GeP_4—A Novel Compound Class with Mixed Li^+ Ionic and Electronic Conductivity. *Chem. Mater.* **2018**, *30*, 6440-6448.

(20) Boyce, J. B.; Huberman, B. A. Superionic Conductors: Transitions, Structures, Dynamics. *Phys. Rep.* **1979**, *51*, 189-265.

(21) Wang, Y.; Richards, W. D.; Ong, S. P.; Miara, L. J.; Kim, J. C.; Mo, Y.; Ceder, G. Design Principles for Solid-State Lithium Superionic Conductors. *Nat. Mater.* **2015**, *14*, 1026.

(22) Carette, B.; Ribes, M.; Souquet, J. L. The Effects of Mixed Anions in Ionic Conductive Glasses. *Solid State Ionics* **1983**, *9-10*, 735-737.

(23) Deng, Y.; Eames, C.; Fleutot, B.; David, R.; Chotard, J.-N.; Suard, E.; Masquelier, C.; Islam, M. S. Enhancing the Lithium Ion Conductivity in Lithium Superionic Conductor (LISICON) Solid Electrolytes through a Mixed Polyanion Effect. *ACS Appl. Mater. Interfaces* **2017**, *9*, 7050-7058.

(24) Eickhoff, H.; Toffoletti, L.; Klein, W.; Raudaschl-Sieber, G.; Fässler, T. F. Synthesis and Characterization of the Lithium-Rich Phosphidosilicates $Li_{10}Si_2P_6$ and $Li_3Si_3P_7$. *Inorg. Chem.* **2017**, *56*, 6688-6694.

(25) Haffner, A.; Bräuniger, T.; Johrendt, D. Supertetrahedral Networks and Lithium-Ion Mobility in Li_2SiP_2 and $LiSi_2P_3$. *Angew. Chem., Int. Ed.* **2016**, *55*, 13585-13588.

(26) *WinXPOW V3.0.2.1.*, 3.0.2.1.; STOE & Cie GmbH: Darmstadt, Germany, 2011.

(27) Hoelzel, M.; Senyshyn, A.; Juenke, N.; Boysen, H.; Schmahl, W.; Fuess, H. High-Resolution Neutron Powder Diffractometer SPODI at Research Reactor FRM II. *Nucl. Instrum. Methods Phys. Res. A* **2012**, *667*, 32-37.

(28) Rodriguez-Carvajal, J.; Gonzales-Platas, J. *FullProf Suite 2. 05*, Institute Laue-Langevin Grenoble: France, 2011.

(29) Momma, K.; Izumi, F. VESTA 3 for Three-Dimensional Visualization of Crystal, Volumetric and Morphology Data. *J. Appl. Crystallogr.* **2011**, *44*, 1272-1276.

(30) Sheldrick, G. M. Crystal Structure Refinement with SHELXL. *Acta Crystallogr., Sect. C: Struct. Chem.* **2015**, *71*, 3-8.

(31) *Proteus Thermal Analysis V4.8.2*, Netzsch-Gerätebau GmbH: Selb, 2006.

(32) Yeandel, S. R.; Scanlon, D. O.; Goddard, P. Enhanced Li-Ion Dynamics in Trivalently Doped Lithium Phosphidosilicate Li_2SiP_2: A Candidate Material as a Solid Li Electrolyte. *J. Mater. Chem. A* **2019**, *7*, 3953-3961.

(33) Clark, S. J.; Segall, M. D.; Pickard, C. J.; Hasnip, P. J.; Probert, M. J.; Refson, K.; Payne, M. C. First Principles Methods Using CASTEP. *Z. Kristallogr.* **2005**, *220*, 567-570.

(34) VandeVondele, J.; Krack, M.; Mohamed, F.; Parrinello, M.; Chassaing, T.; Hutter, J. Quickstep: Fast and Accurate Density Functional Calculations Using a Mixed Gaussian and Plane Waves Approach. *Comput. Phys. Commun.* **2005**, *167*, 103-128.

(35) Zintl, E.; Brauer, G. Konstitution der Lithium-Wismut-Legierungen: 14. Mitteilung über Metalle u. Legierungen. *Z. Elektrochem.* **1935**, *41*, 297-303.

(36) Dong, Y.; DiSalvo, F. J. Reinvestigation of Trilithium Phosphide, Li_3P. *Acta Crystallogr., Sect. E: Struct. Rep. Online* **2007**, *63*, i97-i98.

(37) Zeilinger, M.; Benson, D.; Häussermann, U.; Fässler, T. F. Single Crystal Growth and Thermodynamic Stability of $Li_{17}Si_4$. *Chem. Mater.* **2013**, *25*, 1960-1967.

(38) Franke, D.; Hudalla, C.; Maxwell, R.; Eckert, H. Phosphorus-31-Cadmium-113 and Phosphorus-31-Silicon-29 CP/MAS-NMR in Inorganic Semiconductors. *J. Phys. Chem.* **1992**, *96*, 7506-7509.

(39) Vočadlo, L.; Knight, K. S.; Price, G. D.; Wood, I. G. Thermal Expansion and Crystal Structure of FeSi between 4 and 1173 K Determined by Time-of-Flight Neutron Powder Diffraction. *Phys. Chem. Miner.* **2002**, *29*, 132-139.

(40) Senyshyn, A.; Boysen, H.; Niewa, R.; Banys, J.; Kinka, M.; Ya, B.; Adamiv, V.; Izumi, F.; Chumak, I.; Fuess, H. High-Temperature Properties of Lithium Tetraborate $Li_2B_4O_7$. *J. Phys. D: Appl. Phys.* **2012**, *45*, 175305.

(41) Baran, V.; Dolotko, O.; Mühlbauer, M. J.; Senyshyn, A.; Ehrenberg, H. Thermal Structural Behavior of Electrodes in Li-Ion Battery Studied In Operando. *J. Electrochem. Soc.* **2018**, *165*, A1975-A1982.

(42) Hodge, I. M.; Ingram, M. D.; West, A. R. Impedance and Modulus Spectroscopy of Polycrystalline Solid Electrolytes. *J. Electroanal. Chem.* **1976**, *74*, 125-143.

(43) Gilmore, C. Maximum Entropy and Bayesian Statistics in Crystallography: A Review of Practical Applications. *Acta Crystallogr., Sect. A: Found. Crystallogr.* **1996**, *52*, 561-589.

(44) Momma, K.; Ikeda, T.; Belik, A. A.; Izumi, F. Dysnomia, a Computer Program for Maximum-Entropy Method (MEM) Analysis and its Performance in the MEM-Based Pattern Fitting. *Powder Diffr.* **2013**, *28*, 184-193.

(45) Humphrey, W.; Dalke, A.; Schulten, K. VMD: Visual Molecular Dynamics. *J. Mol. Graphics* **1996**, *14*, 33-38.

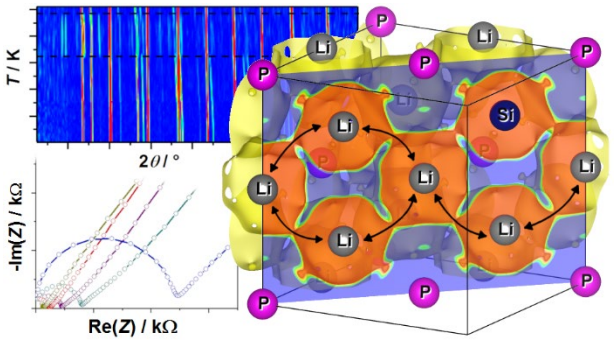
T / K
2θ / °
-Im(Z) / kΩ
Re(Z) / kΩ
P
Li
Si